

Accepted Manuscript

Oxygen crossover effect on palladium and platinum based electrocatalysts during formic acid oxidation studied by scanning electrochemical microscopy

Juan V. Perales-Rondón, Enrique Herrero, José Solla-Gullón, Carlos M. Sánchez-Sánchez, Vincent Vivier



PII: S1572-6657(16)30751-2
DOI: doi: [10.1016/j.jelechem.2016.12.049](https://doi.org/10.1016/j.jelechem.2016.12.049)
Reference: JEAC 3045

To appear in: *Journal of Electroanalytical Chemistry*

Received date: 3 October 2016
Revised date: 16 December 2016
Accepted date: 30 December 2016

Please cite this article as: Juan V. Perales-Rondón, Enrique Herrero, José Solla-Gullón, Carlos M. Sánchez-Sánchez, Vincent Vivier, Oxygen crossover effect on palladium and platinum based electrocatalysts during formic acid oxidation studied by scanning electrochemical microscopy. The address for the corresponding author was captured as affiliation for all authors. Please check if appropriate. *Jeac*(2016), doi: [10.1016/j.jelechem.2016.12.049](https://doi.org/10.1016/j.jelechem.2016.12.049)

This is a PDF file of an unedited manuscript that has been accepted for publication. As a service to our customers we are providing this early version of the manuscript. The manuscript will undergo copyediting, typesetting, and review of the resulting proof before it is published in its final form. Please note that during the production process errors may be discovered which could affect the content, and all legal disclaimers that apply to the journal pertain.

Oxygen Crossover Effect on Palladium and Platinum
Based Electrocatalysts During Formic Acid Oxidation
Studied by Scanning Electrochemical Microscopy

Juan V. Perales-Rondón^{a,b}, Enrique Herrero^b, José Solla-Gullón^b, Carlos M. Sánchez-Sánchez^{*a}, Vincent Vivier^a

^aSorbonne Universités, UPMC Univ Paris 06, CNRS, Laboratoire Interfaces et Systèmes Electrochimiques, 4 place Jussieu, F-75005, Paris, France.

^bInstituto Universitario de Electroquímica, Universidad de Alicante, Ap. 99, 03080, Alicante, Spain

* Corresponding author: Tel.: +33 1 44 27 41 58

E-mail address: carlos.sanchez@upmc.fr

Abstract

The electrocatalytic activity towards formic acid oxidation reaction (FAOR) in the presence of simultaneous oxygen reduction reaction (ORR) displayed by 5 different metallic nanoparticles (NPs) (Pt₁₀₀, Pt₇₅Pd₂₅, Pt₅₀Pd₅₀, Pt₂₅Pd₇₅ and Pd₁₀₀) was studied and compared using chronoamperometry and the micropipette delivery/substrate collection (MD/SC) mode of the scanning electrochemical microscopy (SECM). This is of special interest for understanding the O₂ crossover effect in direct formic acid fuel cells (DFAFCs) and to search highly selective electrocatalysts useful in mixed-reactant fuel cells (MRFCs). A detailed analysis of the SECM results in comparison with chronoamperometry demonstrates, for the first time, the relevant role played by dissolved O₂ in solution on the Pd₁₀₀ NPs deactivation during FAOR, which cannot be explained neither by the specific adsorption of dichloroethane (DCE) on Pd nor by a simple addition of two opposed currents coming from simultaneous FAOR and ORR. Two main mechanistic factors are proposed for explaining the different sensitivity towards O₂ presence in solution during FAOR when comparing Pd- and Pt-rich catalysts. On the one hand, the relevance of H₂O₂ production (ORR byproduct) and accumulation on Pd NPs, which alters its performance towards FAOR. On the other hand, the predominance of the poisoning pathway forming CO_{ads} during FAOR on Pt NPs, whose oxidation is facilitated in the presence of traces of O₂. Interestingly, the deactivation effect displayed on Pd₁₀₀ NPs during FAOR due to the H₂O₂ generation and accumulation becomes negligible if a convective regime is applied in solution. SECM is proved as a fast and powerful technique for studying O₂ crossover effect in different electrocatalysts and for identifying highly selective electrocatalysts candidates for MRFCs. In particular, among the samples evaluated, Pt₇₅Pd₂₅ NPs present the

highest average performance for FAOR in 0.5 M H₂SO₄ solution in the presence of O₂ within the potential range under study (0.3-0.7 V vs RHE).

Keywords: Crossover, FAOR, ORR, fuel cells, SECM

This article is dedicated to the memory of Prof. Antonio Aldaz Riera, a great mentor in science and life.

ACCEPTED MANUSCRIPT

Highlights:

- SECM as a proper diagnostic tool to evaluate electrocatalysts in the presence of reactants crossover.
- Simultaneous FAOR and ORR on Pd, Pt and Pd-Pt alloyed nanoparticles imaged by SECM.
- Pd electrode deactivation during FAOR due to the role of O₂ crossover.
- Pt₇₅Pd₂₅ nanoparticles display the highest performance for FAOR in the presence of O₂.

ACCEPTED MANUSCRIPT

1. Introduction

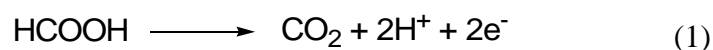
Fuel cells have attracted a lot of attention, from their first description as a gas voltaic battery by W.R. Grove on the 19th century [1,2]. This is because fuel cells, as well as other electrochemical devices, are able to convert chemical energy into electrical energy in one single step and they do not need to produce firstly mechanical work and secondly electrical energy as the internal combustion engine does [3]. There are many different types of fuel cells that may be classified either by their operation temperature or by the type of electrolyte used. Nevertheless, almost all low-temperature fuel cells ($T < 200$ °C) use a conventional two-compartment reactor separated by an ion exchange membrane where the fuel and the oxidant flows are kept apart and directly fed into the anode and cathode chambers, respectively. However, crossover effects in different types of conventional fuel cells have been already described in the literature, since reactants crossover can lead to significant performance degradation, a non-negligible crossover current contribution and an important fuel cell voltage and power output diminution. A lot of attention has been paid to the permeation of fuels such as methanol [4], formic acid [5,6] and hydrogen [7] from the anode to the cathode side in conventional fuel cells. In particular, fuel crossover represents a major issue for direct methanol fuel cells (DMFCs) [8-10], since this problem accounts for one of their major performance losses. Moreover, this fact limits the maximum methanol concentration used at the anode side, since methanol crossover provokes cathode deactivation by CO poisoning. More recently, oxygen crossover in non-aqueous Li-air batteries, which can be considered as a reversible half-fuel cell, has also become a relevant issue limiting the market penetration of this type of technology, since one of their main limitations at present is the formation of unwanted lithium derivatives (Li_2CO_3 and LiOH) caused by O_2 crossover into the anode side [11,12]. Alternatively, other types of reactors eliminating

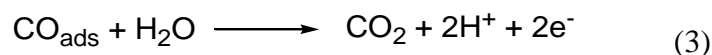
the ionic membrane have been recently proposed in fuel cells for avoiding high cost, degradation and ohmic losses due to the use of those membranes. For instance, the Swiss-roll mixed-reactant fuel cell (MRFC) [13,14], where the ion exchange membrane has been substituted by a highly porous separator and a single mixture of fuel and oxidant feeds simultaneously anode and cathode. The key issue for the success of those systems is to achieve high selectivity of the anode and cathode electrocatalysts to avoid mixed-potentials at both electrodes and fuel-cell voltage degradation. This means electrocatalysts with high tolerance to the presence of a high concentration of either the fuel or the oxidant, for cathode and anode, respectively. Therefore, in both cases, either to study the role of reactants crossover on the corresponding counterpart electrocatalyst activity in conventional fuel cells or to find novel highly selective electrocatalysts useful in MRFCs, it is necessary to identify a diagnostic tool, which should be able to evaluate electrocatalyst performance under those specific experimental conditions.

A broad range of electrochemical techniques have been already used to study different aspects present in fuel cells and batteries. For instance, impedance techniques have been widely used to determine the state-of-charge and electrodes stability in primary and secondary batteries [15,16]. More recently, new electrochemical scanning probe microscopies [17-19] have been incorporated too, since there is a significant demand of *in-situ* methods for simultaneous evaluation of electrodes surface properties and chemical activity. In particular, scanning electrochemical microscopy (SECM) [20,21] has become a powerful electroanalytical technique that has been already successfully applied to study Li-ion batteries [22,23] and electrocatalyst performance for different fuel cell reactions [24] such as oxygen reduction (ORR)[25-31], oxygen evolution (OER) [32-34], carbon dioxide reduction (CRR)[35], methanol oxidation (MOR)[36] and formic acid oxidation (FAOR) [36-38], as well as a high-throughput

technique applied to the combinatorial screening of mixed and alloyed electrocatalytic materials [39-41]. However, they are very scarce examples where SECM have been already used to study either electrocatalysts tolerance to the presence of the counterpart reactant or highly selective electrocatalysts useful in MRFCs. So far, only the use of the tip generation/substrate collection (TG/SC) mode of SECM for studying methanol tolerance of Pt and Pd-Co ORR electrocatalysts as a function of applied potential have been reported [42]. In this context, the direct formic acid fuel cell (DFAFC) [43,44], which is based on the electrochemical oxidation of formic acid (HCOOH) to CO₂ at the anode ($E^\circ = -0.199$ V or -0.25 V vs SHE depending on the HCOOH reference state used for the thermodynamic calculation of the standard potential (aqueous or liquid, respectively) [45]) and ORR at the cathode ($E^\circ = 1.229$ V vs SHE) represents an attractive system to study electrocatalysts selectivity and tolerance facing reactants crossover.

FAOR on pure Pt may follow two main reaction routes: through a direct via, which produces CO₂ as main product and represents the desirable pathway (dehydrogenation, reaction 1) and/or through a poisoning pathway (dehydration, reaction 2) by forming CO, which remains strongly adsorbed on the platinum surface and blocks the reaction of interest, unless a positive enough potential is reached for desorbing and oxidizing CO from the Pt surface (reaction 3). In contrast, FAOR on pure Pd mainly follows the active intermediate route (reaction 1) avoiding CO formation and providing a much higher catalytic activity at lower overpotentials than on Pt electrodes [46,47]. For this reason, Pd and Pd-based materials are considered as the state-of-the-art anode catalysts in DFAFCs [48-51].





The most studied case in DFAFCs is the HCOOH crossover effect during ORR, which has been already reported as not truly relevant for the DFAFCs performance [5,6]. Nevertheless, the case of oxygen crossover effect during FAOR on Pd, Pt and Pd-Pt alloys, which we study herein is, so far, a non-described phenomenon in electrocatalysts for FAOR. Therefore, the main goal of this article is to mimic the effect of O₂ crossover from the cathode side towards the anode side in DFAFCs, using the micropipette delivery/substrate collection (MD/SC) mode of SECM, which is based on the transfer of a neutral species by diffusion across an immiscible liquid/liquid interface as sketched for HCOOH in Figure 1 [36,38,52]. It is worth noting that the acidic solution used as aqueous phase outside the micropipette should not be totally deaerated in order to study the effect of simultaneous reactions, FAOR and ORR, on Pd, Pt and Pd-Pt alloys.

2. Experimental

Chemicals and Electrodes

Most chemicals were ACS reagent grade supplied by Sigma-Aldrich and were used without further purification: 1,2-dichloroethane (CH₂Cl-CH₂Cl, DCE) anhydrous 99.8%, octyltriethoxysilane 97.5%, polyethylene glycol dodecyl ether (Brij[®] 30), n-heptane, sodium borohydride (NaBH₄) 99.99%, K₂PdCl₄ 99.99%, H₂PtCl₆•6H₂O 99.99% (37.50% in Pt). However, H₂SO₄ Suprapur[®] 96% and HCOOH 98 % were supplied by Merck, glassy carbon (GC) plates 1 mm thick (type 2) from Alfa Aesar and Ar gas ≥ 99.9998 purity was supplied by Air Liquide. All aqueous solutions were prepared with ultrapure water (18.2 MΩ cm at 25 °C, Purelab Ultra system, Elga-Vivendi).

Synthesis of Pt, Pd and PtPd alloyed nanoparticles (NPs)

5 different types of quasi-spherical Pt-Pd NPs (Pt_{100} , $\text{Pt}_{75}\text{Pd}_{25}$, $\text{Pt}_{50}\text{Pd}_{50}$, $\text{Pt}_{25}\text{Pd}_{75}$ and Pd_{100}) were synthesized by reduction of either H_2PtCl_6 and/or K_2PdCl_4 precursors with NaBH_4 using a water in oil (w/o) microemulsion of water/polyethylene glycol-dodecylether (BRIJ[®] 30)/n-heptane [^{47,53}]. The percentage of surfactant in volume represented 16.5% of the total microemulsion volume. The concentration of H_2PtCl_6 , K_2PdCl_4 and NaBH_4 was 0.1, 0.1, 1.0 M, respectively. For preparation of PtPd alloyed NPs, an aqueous solution containing both precursors ($\text{H}_2\text{PtCl}_6 + \text{K}_2\text{PdCl}_4$) with the proper atomic ratio of both elements was employed. In order to have micelles with the same size, the molar ratio water to surfactant was kept constant, which approximately ensures constant NP size in all cases (3 - 4 nm average NPs size). After complete reduction of the metallic precursors, which took place in a few minutes, acetone was added to the solution to cause phase separation and NPs flocculation. Finally, all metallic NPs synthesized were washed with acetone as has been described in previous works [⁵⁴] in order to eliminate adsorbed surfactant and were dispersed in ultra-pure water giving as a result 5 independent NPs suspensions.

Voltammetric and chronoamperometric studies

Cyclic voltammetry (CV) and chronoamperometry experiments were carried out in a conventional electrochemical glass cell using a three-electrode configuration at room temperature with (1000 rpm) or without electrode rotation. The counter and the reference electrodes were a Pt wire (0.5 mm diameter) and a reversible hydrogen electrode (RHE), respectively. All NPs were studied by depositing 4 μL of each NPs suspension either on a gold collector for static measurements or on a GC rotating disc electrode (RDE) for reaching a laminar convection regime. All electrode potentials in

this work are quoted vs. *RHE*. The electrode potential was controlled either with a CHI 760E potentiostat (CHI Instruments) or with a multi-channel VMP3 potentiostat (BioLogic), working with an NStat configuration (1 counter, 1 reference and 5 simultaneous working electrodes). CVs for electrochemical surface area (ECSA) quantification were carried out in a deaerated 0.5 M H₂SO₄ solution. Chronoamperometries for studying the electrocatalytic activity for FAOR were carried out in: *i*) deaerated 0.01 M HCOOH and 0.5 M H₂SO₄ solution, *ii*) deaerated 0.01 M HCOOH, 0.088 M DCE and 0.5 M H₂SO₄ solution and *iii*) air saturated 0.01 M HCOOH and 0.5 M H₂SO₄ solution. An electrochemical pre-treatment for removing the CO_{ads} accumulated at the electrode surface from previous FAOR experiments was performed before starting each new chronoamperometry. This consists in holding the electrode potential at 0.9 V for 5 s, since CO_{ads} on the Pd surface requires a bit more positive potential than on Pt for being totally oxidized to CO₂ [⁴⁷].

Electrochemical surface area (ECSA) of Pt, Pd and PtPd alloyed NPs

The ECSA for all 5 types of NPs was electrochemically determined by depositing 2 μ L of each NPs suspension on a gold current collector and quantifying the charge involved under the voltammetric peaks corresponding to the hydrogen desorption within the hydrogen underpotential deposition (UPD) region (between 0.05 and 0.45 V for Pt and Pt alloyed NPs and between 0.1 and 0.5 V for Pd NPs) corrected by subtracting the double-layer contribution [⁵⁵]. For this purpose, the corresponding CV was performed for each type of synthesized NP in a 0.5 M H₂SO₄ deaerated solution at scan rate 50 mV s⁻¹, as it is shown in Figure 2. 210 μ C cm⁻² was adopted as the calibration charge density for the desorption of a complete monolayer of H atoms on polyoriented Pt or Pd electrodes [⁵⁶]. Before ECSA evaluation, an additional cleaning procedure for all 5 types

of synthesized NPs was performed by adsorbing CO at the NPs surface [38,53]. After that, a linear voltammetry at 20 mV s⁻¹ with an upper potential limit of 0.9 V was performed for a complete electrochemical oxidation-stripping of CO from the NPs surface [57]. All 5 types of NPs were suspended in water and normalized for exhibiting equal specific surface area (0.035 cm² μL⁻¹).

Preparation of electrocatalyst arrays of Pt, Pd and PtPd alloyed NPs

The NPs array preparation is described elsewhere [28,52] and the specific array pattern (5 spots in 2 identical rows separated by 700 μm from center to center) used here is schematically described in Figure 3. This was prepared by dispensing all 5 metallic NPs dispersed in water using a picoliter solution dispenser CHI 1550A from CHI Instruments. All 5 types of NPs were dispensed on a conductive flat current collector of GC (1.5 cm x 1.5 cm), which has been selected since is totally inactive for ORR and FAOR within the potential range under study. Each NPs suspension was sonicated for 2 min before charging the dispenser to avoid NPs agglomeration. A total of 160 drops of each type of metallic NPs suspension were dispensed in 8 successive series of 20 drops each, allowing the water solvent to be evaporated before each new series of drops was added. The average spot size obtained was between 200 and 250 μm in diameter.

Glass Micropipette Fabrication

The micropipettes were prepared by pulling borosilicate capillaries with O.D.: 1.5 mm and I.D.: 1.0 mm and length of 90 mm using a laser-based puller P-2000 from Sutter Instrument Co. Micropipettes with an internal opening diameter of 30 μm were routinely fabricated. Micropipettes exact diameter was checked using an optical microscope BA200 from Motic Co. The inner wall of the micropipettes was made

hydrophobic to avoid aqueous solution penetration within the micropipette by filling it with octyltriethoxysilane overnight and finally, drying it exhaustively by pumping air through following an standard protocol [^{36,52,58}]. Then, those micropipettes were loaded with a liquid mixture 50:50 HCOOH:DCE (v/v) before starting electrocatalyst SECM imaging.

Scanning electrochemical microscopy (SECM) imaging

All SECM images were carried out using the MD/SC working mode of SECM using either a CHI 910B or a 920D microscope from CHInstruments and a three-electrode configuration at room temperature. The electrochemical cell employed was built in Teflon with an 8 mm diameter aperture for scanning the substrate electrode. This is an open electrochemical cell, which does not allow total suppression of O₂ in solution. A platinum wire, 0.5 mm diameter, was used as a counter electrode and a commercial Hg/Hg₂SO₄ (K₂SO₄ sat.) electrode within a Luggin capillary as reference. Nevertheless, all potential values presented herein have been referred to *RHE* ($E_{\text{Hg}/\text{Hg}_2\text{SO}_4} = +0.64 \text{ V vs. } RHE$ for the pH value of the solutions employed). Before FAOR imaging any tilt on the electrocatalyst array substrate was eliminated in order to avoid crushing the glass micropipette while scanning. This is achieved by performing a series of approach curves using a gold ultramicroelectrode (UME) built by heat sealing under vacuum a gold wire in a flint glass capillary as described elsewhere [²⁰]. This procedure consists in approaching a gold UME of 25 μm diameter to the array substrate surface at three different locations. The gold UME is kept at a potential negative enough to perform ORR under steady-state conditions. Controlling the ratio between the steady-state current and the final current of the gold UME when is approaching the GC surface, it is possible to establish a controlled tip-substrate distance. In particular, we select

stopping the UME approach when the distance between the UME and the surface is equivalent to the UME radius (12.5 μm) [20]. This approach is repeated at three different locations on the GC surface, making a triangle between these three points. The electrocatalyst array substrate tilt is considered corrected when reaches the following condition: $\Delta z/\Delta x(\text{or } \Delta y) < (1.5 \mu\text{m}/1 \text{ mm})$. Then, the gold UME is replaced by a glass micropipette filled with a solution of HCOOH:DCE (50:50), which is slowly approached until it touches the GC surface, but avoiding to crush it. After this, the micropipette is retracted 50 μm in Z direction. Then, the micropipette scans at constant distance the array surface in the XY plane, meanwhile the species of interest (HCOOH) is delivered within the bulk solution by crossing the liquid-liquid interface between two immiscible phases, DCE and H₂O, in this case. The current collection for FAOR (difference between the maximum oxidation current displayed at the catalyst spot location and the background current at the same scanned line in the SECM image at a given tip-substrate distance) is calculated to quantitatively compare the catalytic activity of all different materials studied by SECM [38,59] (see later Table 1).

All SECM images were collected after performing an electrochemical pre-treatment for removing the CO_{ads} accumulated at the electrode surface from previous FAOR experiments (potential pulse at 0.9 V for 2 s). The electrolyte 0.5 M H₂SO₄ was purged with Ar gas until a low concentration of O₂ in the bulk solution was reached (0.10 mM, 40% of the initial O₂ concentration in air saturated solution [60]). This O₂ concentration in solution was experimentally determined by measuring the electrochemical steady state current for ORR at -0.05 V provided by a gold UME after purging with Ar gas the 0.5 M H₂SO₄ solution within the SECM cell. Moreover, an Ar blanket was kept above the solution during SECM imaging. The tip scan rate was 125 $\mu\text{m s}^{-1}$, using increments of 25 μm each 0.2 s.

3. Results and discussion

First of all, the catalytic activity for FAOR of all 5 metallic NPs synthesized is individually evaluated by chronoamperometry at 3 different potentials (0.3 V, 0.5 V and 0.7 V) in a low concentrated HCOOH solution (0.01 M) in order to achieve a similar concentration to that found in the SECM experiment. Figure 4 shows the comparison of all 5 oxidation current densities displayed by Pt, Pd and PtPd alloyed NPs after 600 s. This comparison allows to identify the most active electrocatalyst for FAOR under steady-state conditions at each given potential. In particular, Pd₁₀₀ and secondly Pt₂₅Pd₇₅ NPs exhibit the highest activity at 0.3 V (figure 4A), meanwhile Pt₁₀₀ NPs exhibit a negligible activity at the same potential, due to CO poisoning [61]. In contrast, Pt₇₅Pd₂₅ and secondly Pt₁₀₀ NPs exhibit the maximum activity at 0.5 and 0.7 V (figures 4B and 4C), meanwhile, Pd₁₀₀ NPs show a negligible oxidation current at those potentials. These results are in agreement with those already published in the literature [62-64]. Nevertheless, they correspond to the electrocatalysts activity towards FAOR in the total absence of any other competitive reaction.

In contrast, Figure 5 displays SECM images for simultaneous FAOR and ORR under steady-state conditions on the electrocatalyst array formed by Pt, Pd and PtPd alloyed NPs schematically shown in Figure 3. These SECM images are also collected at 3 different potential values, namely, 0.3 V, 0.5 V and 0.7 V. Unlike the behavior observed in the chronoamperometric tests presented in Figure 4, Pt₅₀Pd₅₀ is the most active electrocatalyst spot at 0.3 V ($I_{\text{collected}} = 97$ nA), whereas Pt₇₅Pd₂₅ is the most active sample at 0.5 ($I_{\text{collected}} = 75$ nA) and 0.7 V ($I_{\text{collected}} = 56$ nA). Table 1 summarizes the oxidation current collected on each catalytic spot from the SECM images shown in Figure 5 as a function of applied potential. As can be seen, SECM catalytic activity

results at 0.3 V differ from those obtained by chronoamperometry (Figure 4A). Nevertheless, there is a common feature, Pt₇₅Pd₂₅ and secondly Pt₁₀₀ electrocatalyst spots exhibit the highest catalytic activity at 0.5 and 0.7 V in both cases (figures 4B, 4C and 5). Furthermore, in all 3 SECM images, the background current corresponds to a reduction current on the array. In fact, the reason for that behavior is that active electrocatalyst spots for FAOR provide some oxidation current when the micropipette fluxes HCOOH on top of them, however, this oxidation current is not large enough to overcome the initial reduction current coming from the ORR and only produces a diminution in the background reduction current. This behavior is unexpected taking into account the important difference in local concentration between both electroactive species, O₂ and HCOOH. Bulk O₂ concentration in solution is very low (0.1 mM) and local HCOOH concentration coming out from the micropipette is expected to be much more important, since HCOOH presents high affinity toward the aqueous phase. Thus, we assume a fast HCOOH transfer across the liquid-liquid interface in the micropipette, which is the case for most similar neutral molecules [³⁶]. It means a low partition coefficient, K (≈ 0.01), which is defined as the ratio between backward and forward rate constants (k_b/k_f) of the molecule coming out from the micropipette. Therefore, this comparison between catalytic activity for FAOR (Figure 4) and simultaneous FAOR and ORR (Figure 5) raises up a huge impact of O₂ crossover effect during FAOR. However, the impact of this effect is very different on Pd- and Pt-rich electrocatalysts and this is particularly relevant on Pd-rich electrocatalysts, since Pd₁₀₀ and Pt₂₅Pd₇₅ electrocatalyst spots display a much lower HCOOH oxidation current than Pt-rich electrocatalysts under the same experimental conditions (SECM image, Figure 5). In spite of the fact that HCOOH local concentration should be at least two orders of magnitude larger than that of O₂ under those experimental conditions and thus, an

oxidation net current would be expected in the SECM images, which is not the case in Figure 5. Additionally, it is important to rule out the potential contamination effect associated with the leakage of DCE coming out from the micropipette during SECM images, in order to demonstrate the relevant role of the O_2 presence in solution during FAOR on Pd-rich catalysts. It has been already reported in the literature a strong adsorption of DCE at Pd surface [65], which could partially hinder their catalytic response and justify lower oxidation currents obtained when the MD/SC mode of SECM is used to study those electrocatalysts. Actually, DCE presents a non-negligible solubility in water (8.7 g/L at 20°C [66], which is equivalent to 0.088 M). For this reason, it is feasible that some DCE can get across the micropipette liquid-liquid interface and reach the electrocatalysts surface. Figure 6 presents the same chronoamperometries displayed in Figure 4, but in the presence of 0.088 M DCE in solution. Then, comparing the maximum current density reached in the presence (Figure 6) and absence (Figure 4) of DCE, it is evident that an important drop in catalytic current for all 5 metallic NPs studied is observed when DCE is in solution (Figure 6). Moreover, a faster catalyst deactivation effect is observed for Pd₁₀₀ at 0.3 V and Pt₇₅Pd₂₅ at 0.5 V in presence of DCE, since the current decay does not stop along 600 s. Nevertheless, the most active electrocatalyst as a function of applied potential remains unchanged in all cases (Pd₁₀₀ at 0.3 V and Pt₇₅Pd₂₅ at 0.5 V and 0.7V). Thus, it is demonstrated that the sole presence of DCE in solution is not enough to justify the important difference in catalytic activity reported by SECM when simultaneous FAOR and ORR take place on Pd-rich electrocatalysts. Moreover, our results prove that the accumulation of organic solvent released from the micropipette into the solution may be not negligible in long term experiments, provoking an important quantitative impact,

but it does not qualitatively alter the catalytic activity results obtained by the MD/SC mode of SECM.

Finally, Figure 7 compares the O_2 crossover effect during FAOR on Pd electrocatalysts in the absence (Figure 7A, $\omega = 0$ rpm) and in the presence (Figure 7B, $\omega = 1000$ rpm) of convection in solution. Figure 7 displays the same chronoamperometry at 0.3 V performed in an air saturated 0.5 M H_2SO_4 solution (black plots) for evaluating ORR and a 0.5 M H_2SO_4 solution containing 0.01 M $HCOOH$ saturated by either argon (green plots) or air (red plots) for evaluating FAOR and simultaneous FAOR and ORR, respectively. Thus, figure 7A proves that the O_2 crossover effect during FAOR on Pd cannot be explained by a simple addition of two opposed currents coming from ORR and FAOR. The current decrease (0.044 mA cm^{-2}) observed when simultaneous ORR and FAOR occur on the Pd surface (Figure 7A, red plot) in comparison with the current exclusively provided by FAOR (Figure 7A, green plot) does not correspond to the reduction current provided by ORR ($-0.009 \text{ mA cm}^{-2}$, Figure 7A, black plot). Therefore, the results displayed in Figure 7A confirm the reliability of the SECM results already reported in Figure 5, where Pd_{100} NPs show a relevant decrease in activity for FAOR in the presence of a low concentration of O_2 in solution. In contrast, the same chronoamperometries performed under a laminar convective regime (Figure 7B, $\omega = 1000$ rpm), which does not allow the accumulation of any reaction intermediate or product in the vicinity of the electrode surface, display a negligible O_2 crossover effect during FAOR on Pd, since the current decrease shown when the simultaneous ORR and FAOR occur on the Pd surface (ca. 0.032 mA cm^{-2} , Figure 7B, red and green plots) is actually smaller than the reduction current provided by ORR (-0.08 mA cm^{-2} , Figure 7B, black plot). In conclusion, the negative impact on FAOR due to the O_2 crossover

effect on Pd NPs is only relevant when the products or intermediates formed in one or both reactions (FAOR and ORR) accumulate near the electrode surface.

Regarding the different behavior displayed by Pt- and Pd-rich catalysts, it should be noted that for both electrodes, ORR has reached diffusion limited currents at 0.5 or 0.3 V. Thus, it would be expected that the effect of O₂ on both electrodes were similar. It should be also noted that the chronoamperometric results in Figure 4 show that the currents after 600 s for Pd₁₀₀ at 0.3 V and Pt₁₀₀ at 0.5 V are almost the same, thus the mere superposition of an additional reaction, in this case the ORR, which is under diffusion control, should have resulted in a similar diminution in the currents. However, the current diminution effect during FAOR on Pd NPs is significantly higher. Thus, we propose two main factors for explaining the different sensitivity towards O₂ presence in solution during FAOR when comparing Pd- and Pt- rich catalysts. On the one hand, the different type of product formed during ORR on Pd and Pt, since the H₂O₂ production on Pd is much more relevant than on Pt, being the number of electrons exchanged (*n*) during ORR between 2.85 and 3.60 on Pd and between 3.95 and 4.00 on Pt [27]. Therefore, we propose ORR byproducts (particularly H₂O₂) accumulation on the Pd surface as the responsible of diminishing its FAOR catalytic performance. One of the possible options is a chemical reaction producing no net electron transfer between H₂O₂ accumulated on the Pd surface and HCOOH, which reduces the HCOOH concentration close to the surface. On the other hand, at 0.5 V on Pt, CO is still formed and accumulated on the surface [61], leading to lower currents. It is also known that traces of O₂ facilitate the oxidation of adsorbed CO, and, thus, in the presence of O₂, CO coverage on Pt would be smaller, and higher FAOR activity could be obtained. Then, the reduction current due to the ORR would be compensated by a higher oxidation

current for the FAOR, resulting in a lower diminution. This compensating mechanism is not possible on Pd electrodes, because CO is not effectively formed.

4. Conclusions

The relevant role displayed by O₂ crossover during FAOR specially on Pd NPs is demonstrated here. Depending on the electrocatalyst material and the applied potential, O₂ can be reduced simultaneously with HCOOH oxidation, which in some cases produces an important deactivation of FAOR and reduces the interest of that material as anode in DFAFCs. This deactivation effect displayed by O₂ presence in solution is proved for Pd and Pd-rich electrocatalysts by SECM imaging and it is also verified by conventional chronoamperometry. This fact diminishes the anode efficiency by reactant competition and because of ORR byproducts (particularly H₂O₂) accumulate and react on the anode electrocatalyst surface. However, this phenomenon is not equally evident in all types of electrocatalysts, being Pd much more sensitive to this than Pt, since the H₂O₂ production from ORR is much more relevant on Pd than on Pt. Nevertheless, this negative impact displayed on Pd NPs becomes negligible when the hydrodynamic regime in solution does not allow H₂O₂ accumulation on the Pd NPs surface as have been proved by the RDE measurements (Figure 7B). We believe this conclusion provides a new approach to develop future synthesis of Pd-based electrocatalysts for FAOR, since introducing a co-catalyst next to Pd for activating ORR towards H₂O production ($n = 4$) should provide longer-term activity for FAOR. Actually, we think this may be the reason why some recently published Pd-based electrocatalysts (Pd-Ni₂P/C) outperform Pd anodes in DFAFCs [⁴⁸].

SECM is proved as a fast and powerful technique for studying O₂ crossover effect in different electrocatalysts and for identifying highly selective electrocatalysts

candidates for MRFCs, which represents a key issue for further development of DFAFCs and MRFCs. In particular, among the samples evaluated, Pt₇₅Pd₂₅ NPs present the highest average performance for FAOR in presence of O₂ within the entire potential range under study (0.3-0.7 V) according to the SECM current collected in Table 1. The MD/SC mode of SECM is used to locally provide a constant flux of HCOOH near different electrocatalysts in a low concentrated O₂ aqueous solution. However, this mode of SECM could be also applied to study other molecules of interest such as methanol, ethanol or glycerol.

Acknowledgements

This work was financially supported by CNRS (projet Défi Instrumentation aux limites 2015), MINECO (projects CTQ2013-44083-P and CTQ2013-48280-C3-3-R) and Generalitat Valenciana (project PROMETEOII/2014/013).

TABLES

Table 1. Oxidation current collected on Pt, Pd and PtPd alloyed NPs as a function of applied potential from SECM images shown in Figure 5

E (V) vs RHE	$I_{\text{collected}}$ (nA)	$I_{\text{collected}}$ (nA)	$I_{\text{collected}}$ (nA)	$I_{\text{collected}}$ (nA)	$I_{\text{collected}}$ (nA) ¹
	Pt ₁₀₀	Pt ₇₅ Pd ₂₅	Pt ₅₀ Pd ₅₀	Pt ₂₅ Pd ₇₅	Pd ₁₀₀
0.3	50	92	97	65	
0.5	75	75	47	26	
0.7	51	56	44	27	

¹Oxidation current is not different from background current

FIGURES

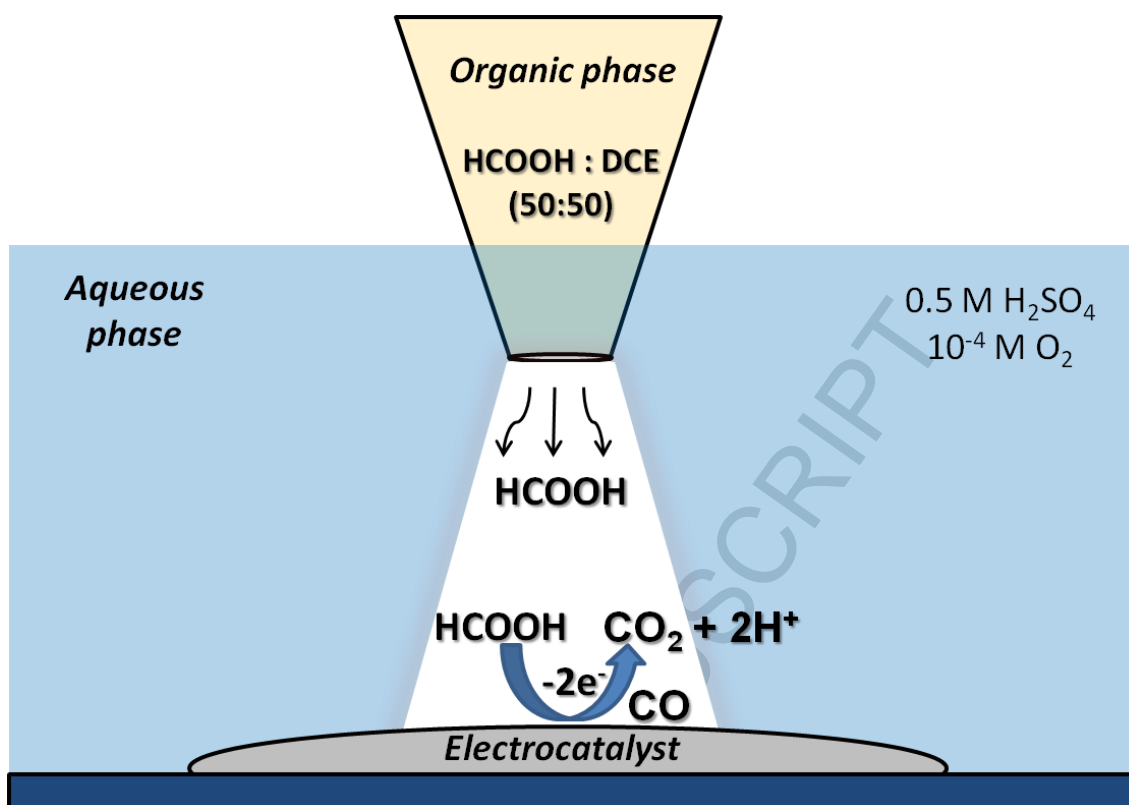


Figure 1. Schematic representation of the conventional MD/SC mode of the SECM applied to the screening of electrocatalysts for the HCOOH oxidation reaction in the presence of O₂ in aqueous solution.

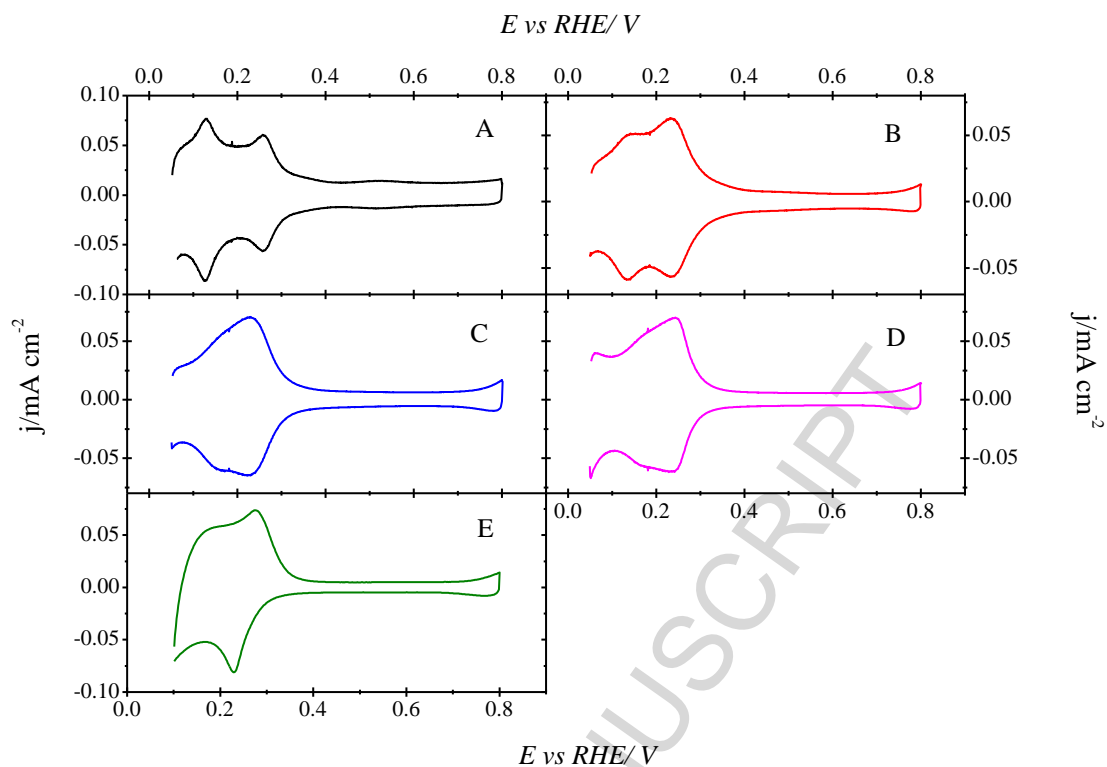


Figure 2. Cyclic voltammeteries for electrochemical surface characterization on synthesized Pt, Pd and Pt-Pd alloyed NPs in deaerated 0.5 M H₂SO₄ solution. (A) Pt₁₀₀; (B) Pt₇₅Pd₂₅; (C) Pt₅₀Pd₅₀; (D) Pt₂₅Pd₂₅ and (E) Pd₁₀₀. Scan rate 50 mV s⁻¹.

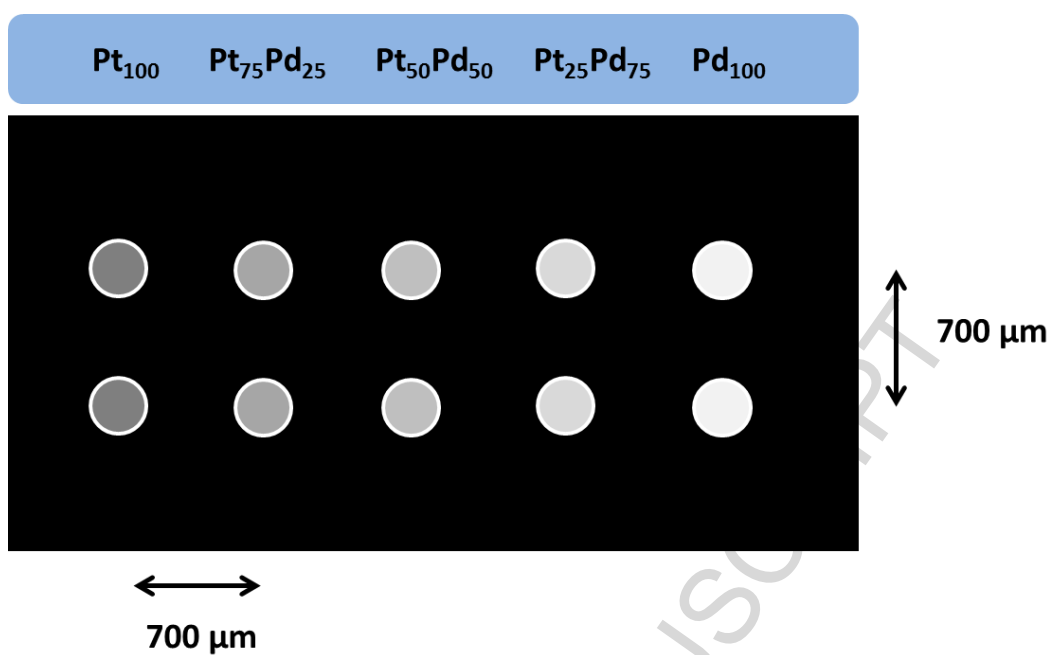


Figure 3. Array pattern of 2 x 5 of Pt, Pd and Pt-Pd alloyed NPs on a glassy carbon substrate.

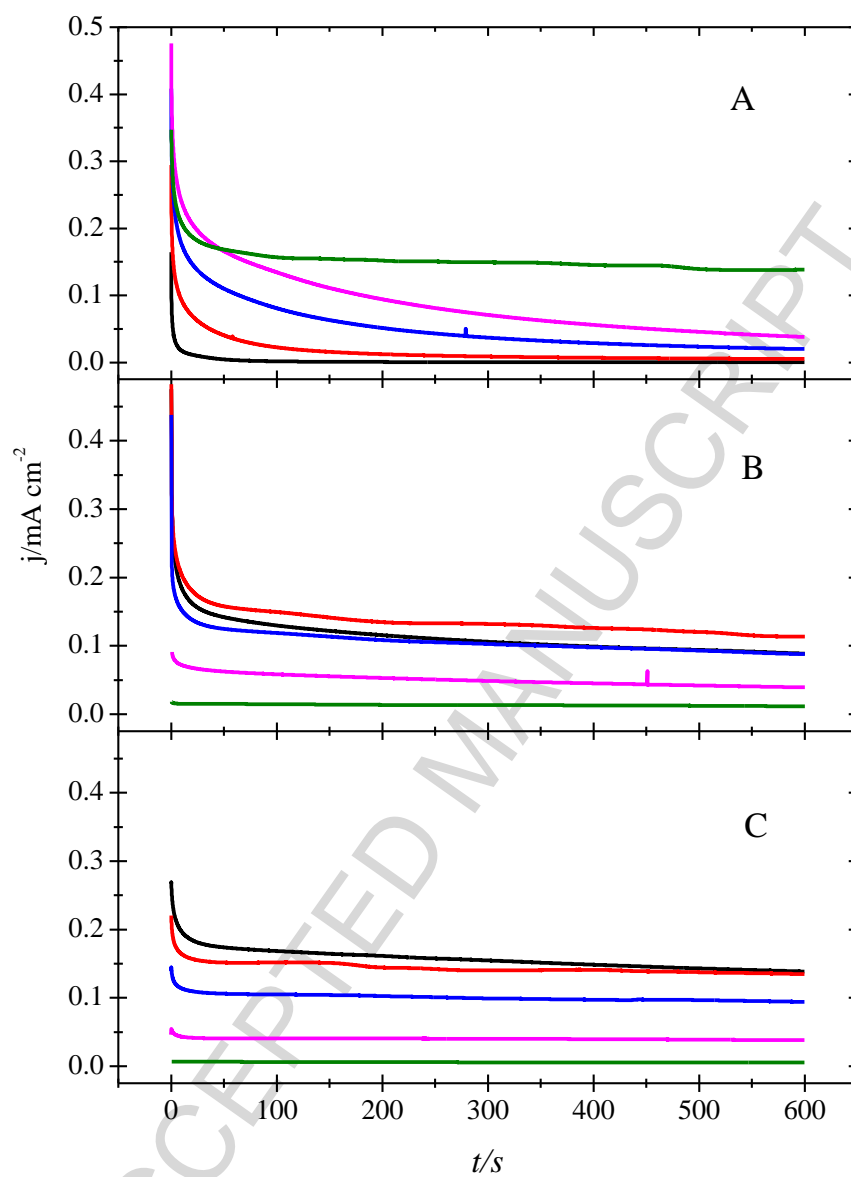


Figure 4. Chronoamperometries of Pt₁₀₀ (black line), Pt₇₅Pd₂₅ (red line), Pt₅₀Pd₅₀ (blue line), Pt₂₅Pd₇₅ (purple line) and Pd₁₀₀ (green line) NPs in argon saturated 0.01 M HCOOH and 0.5 M H₂SO₄ solution at different potentials. A) 0.3 V, B) 0.5 V and C) 0.7 V vs RHE.

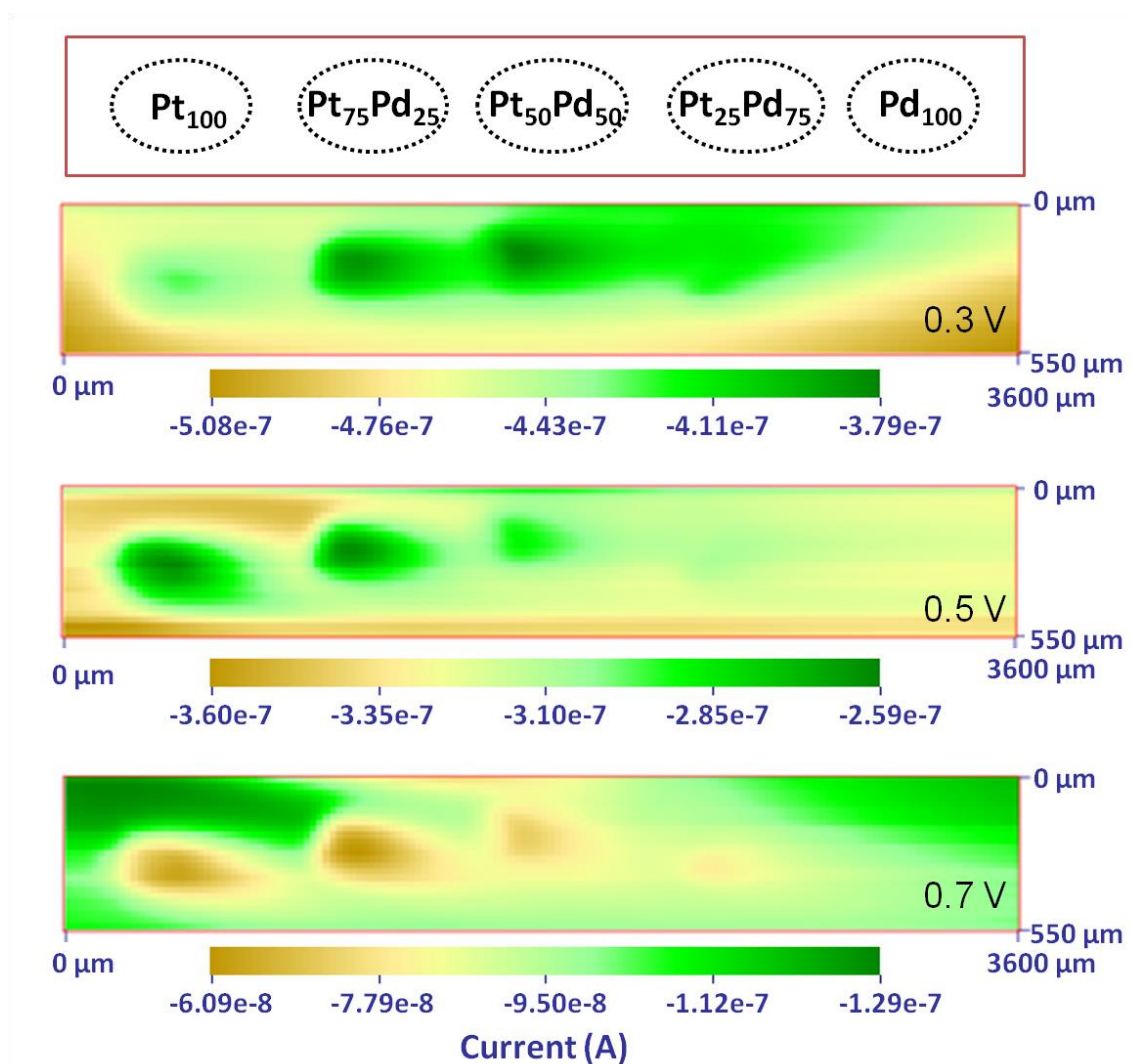


Figure 5. SECM MD/SC images displaying the substrate current for simultaneous FAOR and ORR in 0.5 M H₂SO₄ and 10⁻⁴ M O₂ solution on Pt, Pd and Pt-Pd alloyed NPs. The substrate potential is held constant at 3 different potentials (0.3, 0.5 and 0.7 V vs RHE). The substrate array is formed by spots of 5 different NPs Pt₁₀₀, Pt₇₅Pd₂₅, Pt₅₀Pd₅₀, Pt₂₅Pd₇₅ and Pd₁₀₀. The tip scan rate was 125 μm s⁻¹, using increments of 25 μm each 0.2 s. Tip-substrate distance = 50 μm.

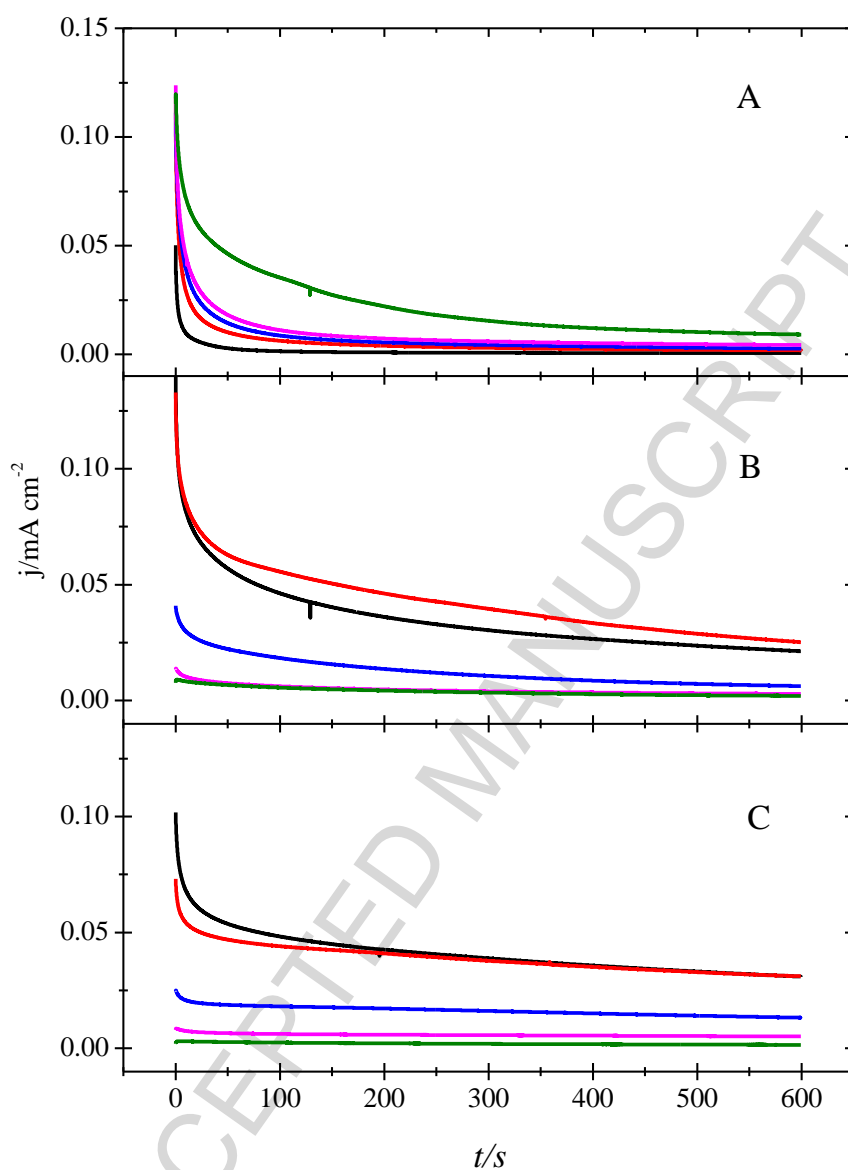


Figure 6. Chronoamperometries of Pt₁₀₀ (black line), Pt₇₅Pd₂₅ (red line), Pt₅₀Pd₅₀ (blue line), Pt₂₅Pd₇₅ (purple line) and Pd₁₀₀ (green line) NPs in argon saturated 0.01 M HCOOH, 0.088 M DCE and 0.5 M H₂SO₄ solution at different potentials. A) 0.3 V, B) 0.5 V and C) 0.7 V vs RHE.

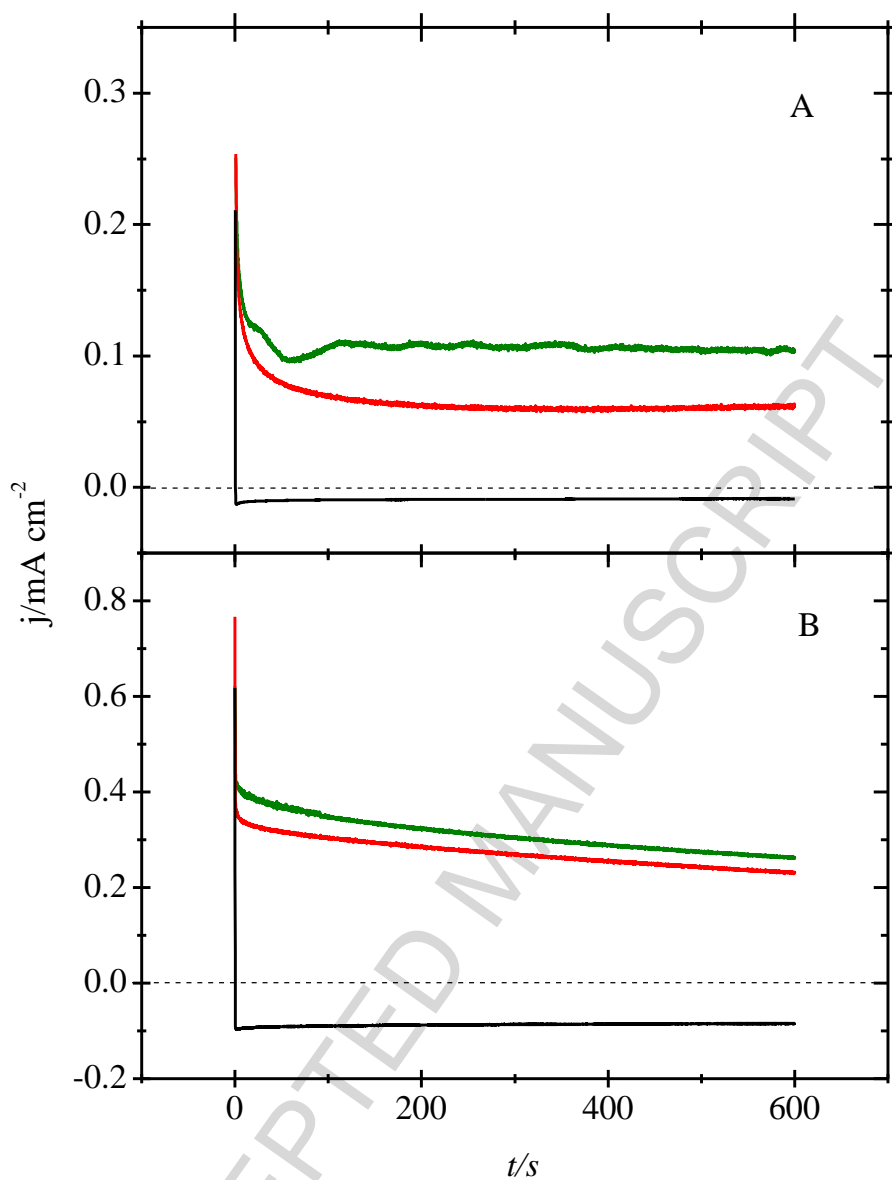


Figure 7. Chronoamperometries at 0.3 V of Pd NPs using a RDE at 0 rpm (A) and 1000 rpm (B). Green plots correspond to an Ar saturated 0.01 M HCOOH + 0.5 M H₂SO₄ solution. Red plots correspond to non deaerated 0.01 M HCOOH + 0.5 M H₂SO₄ solution. Black plots correspond to a non deaerated 0.5 M H₂SO₄ solution.

References

- [¹] L. Carrette, K.A. Friedrich, U. Stimming, Fuel Cells-Fundamentals and Applications, Fuel Cells 1 (2001) 5-39.
- [²] M.K. Debe, Electrocatalyst approaches and challenges for automotive fuel cells, Nature 486 (2012) 43-51.
- [³] A.J. Bard, Inner-sphere heterogeneous electrode reactions. Electrocatalysis and Photocatalysis: The challenge, J. Am. Chem. Soc. 132 (2010) 7559-7567.
- [⁴] A.S. Aricò, S. Srinivasan, V. Antonucci, DMFCs: From fundamental aspects to technology development, Fuel Cells 1 (2001) 133-161.
- [⁵] Y.-W. Rhee, S.Y. Ha, R.I. Masel, Crossover of formic acid through Nafion membranes, J. Power Sources 117 (2003) 35-38.
- [⁶] K.-J. Jeong, C.M. Miesse, J.-H. Choi, J. Lee, J. Han, S.P. Yoon, S.W. Nam, T.-H. Lim, T.G. Lee, Fuel crossover in direct formic acid fuel cells, J. Power Sources 168 (2007) 119-125.
- [⁷] R.P. Brooker, M.P. Rodgers, L.J. Bonville, H.R. Kunz, D.K. Slattery, J.M. Fenton, Influence of trace oxygen in low-crossover proton exchange membrane fuel cells, J. Power Sources 218 (2012) 181-186.
- [⁸] F. Lufrano, V. Baglio, O. Di Blasi, P. Staiti, V. Antonucci, A.S. Aricò, Design of efficient methanol impermeable membranes for fuel cell applications, Phys. Chem. Chem. Phys. 14 (2012) 2718-2726.
- [⁹] J. Prabhuram, T.S. Zhao, H. Yang, Methanol adsorbates on the DMFC cathode and their effect on the cell performance, J. Electroanal. Chem. 578 (2005) 105-112.
- [¹⁰] A. Mehmood, M.A. Scibioh, J. Prabhuram, M.-G. An, H.Y. Ha, A review on durability issues and restoration techniques in long-term operations of direct methanol fuel cells, J. Power Sources 297 (2015) 224-241.

-
- [¹¹] M. Marinaro, P. Balasubramanian, E. Gucciardi, S. Theil, L. Jörissen, M. Wohlfahrt-Mehrens, Importance of reaction kinetics and oxygen crossover in aprotic Li-O₂ batteries based on a dimethyl sulfoxide electrolyte, *ChemSusChem* 8 (2015) 3139-3145.
- [¹²] R.S. Assary, J. Lu, P. Du, X. Luo, X. Zhang, Y. Ren, L.A. Curtiss, K. Amine, The effect of oxygen crossover on the anode of a Li-O₂ battery using an ether-based solvent: Insights from experimental and computational studies. *ChemSusChem* 6 (2013) 51-55.
- [¹³] A. Aziznia, C.W. Oloman, E.L. Gyenge, A Swiss-roll liquid-gas mixed-reactant fuel cell, *J. Power Sources* 212 (2012) 154-160.
- [¹⁴] A. Serov, A. Aziznia, P.H. Benhangi, K. Artyushkova, P. Atanassov, E. Gyenge, Borohydride-tolerant oxygen electroreduction catalyst for mixed-reactant Swill-roll direct borohydride fuel cells, *J. Mater. Chem. A* 1 (2013) 14384-14391.
- [¹⁵] F. Huet, A review of impedance measurements for determination of the state-of-charge or state-of-health of secondary batteries, *J. Power Sources* 70 (1998) 59-69.
- [¹⁶] B. Puga, S. Joiret, V. Vivier, V. Charbonnier, H. Guerrouj, J. Zhang, J. Monnier, C. Fariaut-Georges, M. Latroche, L. Goubault, P. Bernard, Electrochemical properties and dissolution mechanism of A₂Ni₇ hydrides (A=Y, Gd, La-Sm) *ChemElectroChem* 2 (2015) 1321-1330.
- [¹⁷] C. Batchelor-McAuley, E.J.F. Dickinson, N.V. Rees, K.E. Toghill, R.G. Compton, New electrochemical methods, *Anal. Chem.* 84 (2012) 669-684.
- [¹⁸] C. Kranz, Recent advancements in nanoelectrodes and nanopipettes used in combined scanning electrochemical microscopy techniques, *Analyst* 139 (2014) 336-352.
- [¹⁹] N. Ebejer, A.G. Güell, S.C.S. Lai, K. McKelvey, M.E. Snowden, P.R. Unwin, Scanning electrochemical cell microscopy: A versatile technique for nanoscale electrochemistry and functional imaging, *Annu. Rev. Anal. Chem.* 6 (2013) 329-351.

-
- [²⁰] A.J. Bard, M.V. Mirkin (Eds.), *Scanning Electrochemical Microscopy*, second ed., CRC Press, Boca Raton, 2012.
- [²¹] M.V. Mirkin, W. Nogala, J. Velmurugan, Y. Wang, Scanning electrochemical microscopy in the 21st century. Update 1: five years after, *Phys. Chem. Chem. Phys.* 13 (2011) 21196-21212.
- [²²] E. Ventosa, W. Schuhmann, Scanning electrochemical microscopy of Li-ion batteries, *Phys. Chem. Chem. Phys.* 17 (2015) 28441-28450.
- [²³] Z.J. Barton, J. Rodriguez-Lopez, Lithium ion quantification using mercury amalgams as in situ electrochemical probes in nonaqueous media, *Anal. Chem.* 86 (2014) 10660-10667.
- [²⁴] C.M. Sánchez-Sánchez, Studying electrocatalytic activity using scanning electrochemical microscopy, *Electrochem Soc. Interface* 23 (2014) 43-45.
- [²⁵] J.L. Fernández, A.J. Bard, Scanning electrochemical microscopy. 47. Imaging electrocatalytic activity for oxygen reduction in an acidic medium by the tip generation-substrate collection mode, *Anal. Chem.* 75 (2003) 2967-2974.
- [²⁶] Y. Shen, M. Trauble, G. Wittstock, Detection of hydrogen peroxide during electrochemical oxygen reduction using scanning electrochemical microscopy, *Anal. Chem.* 80 (2008) 750-759.
- [²⁷] C.M. Sánchez-Sánchez, A. J. Bard, Hydrogen peroxide production in the oxygen reduction reaction at different electrocatalysts as quantified by scanning electrochemical microscopy. *Anal. Chem.* 81 (2009) 8094-8100.
- [²⁸] C.M. Sánchez-Sánchez, J. Solla-Gullón, F.J. Vidal-Iglesias, A. Aldaz, V. Montiel, E. Herrero, Imaging structure sensitive catalysis on different shape-controlled platinum nanoparticles. *J. Am. Chem. Soc.* 132 (2010) 5622-5624.
- [²⁹] C.M. Sánchez-Sánchez, F.J. Vidal-Iglesias, J. Solla-Gullón, V. Montiel, A. Aldaz, J. M. Feliu, E. Herrero, Scanning electrochemical microscopy for studying electrocatalysis on shape-controlled gold nanoparticles and nanorods. *Electrochim. Acta* 55 (2010) 8252-8257.

- [³⁰] L. Johnson, D.A. Walsh, Tip generation-substrate collection-tip collection mode scanning electrochemical microscopy of oxygen reduction electrocatalysts, *J. Electroanal. Chem.* 682 (2012) 45-52.
- [³¹] H. Deng, P. Peljo, D. Momotenko, F. Cortés-Salazar, T.J. Stockmann, K. Kontturi, M. Opallo, H.H. Girault, Kinetic differentiation of bulk/interfacial oxygen reduction mechanisms at/near liquid/liquid interfaces using scanning electrochemical microscopy. *J. Electroanal. Chem.* 732 (2014) 101-109.
- [³²] A. Minguzzi, M.A. Alpuche-Aviles, J. Rodríguez-Lopez, S. Rondinini, A.J. Bard, Screening of oxygen evolution electrocatalysts by scanning electrochemical microscopy using a shielded tip approach, *Anal. Chem.* 80 (2008) 4055-4064.
- [³³] L.-A. Näslund, C. M. Sánchez-Sánchez, A. S. Ingason, J. Bäckström, E. Herrero, J. Rosen, S. Holmin, The role of TiO₂ doping on RuO₂ coated electrodes for the water oxidation reaction. *J. Phys. Chem. C* 117 (2013) 6126-6135.
- [³⁴] X. Chen, A.J.R. Botz, J. Masa, W. Schuhmann, Characterization of bifunctional electrocatalysts for oxygen reduction and evolution by means of SECM, *J. Solid State Electrochem.* 20 (2016) 1019-1027.
- [³⁵] N. Sreekanth, K.L. Phani, Selective reduction of CO₂ to formate through bicarbonate reduction on metal electrodes: new insights gained from SG/TC mode of SECM, *Chem. Commun.* 50 (2014) 11143-11146.
- [³⁶] C.-L. Lin, J. Rodríguez-López, A.J. Bard, Micropipet delivery-substrate collection mode of scanning electrochemical microscopy for the imaging of electrochemical reactions and the screening of methanol oxidation electrocatalysts, *Anal. Chem.* 81 (2009) 8868-8877.
- [³⁷] C. Jung, C.M. Sánchez-Sánchez, C.-L. Lin, J. Rodríguez-López, A.J. Bard, Electrocatalytic activity of Pd-Co bimetallic mixtures for formic acid oxidation studied by scanning electrochemical microscopy, *Anal. Chem.* 81 (2009) 7003-7008.

-
- [³⁸] J.V. Perales-Rondón, J. Solla-Gullón, E. Herrero, C.M. Sánchez-Sánchez, Enhanced catalytic activity and stability for the electrooxidation of formic acid on lead modified shape controlled platinum nanoparticles, *Appl. Catal. B* 201 (2017) 48-57.
- [³⁹] A.J. Wain, Scanning electrochemical microscopy for combinatorial screening applications: A mini-review, *Electrochem. Commun.* 46 (2014) 9-12.
- [⁴⁰] P. Bertonecello, Advances on scanning electrochemical microscopy (SECM) for energy, *Energy Environ. Sci.* 3 (2010) 1620-1633.
- [⁴¹] J.L. Fernández, D.A. Walsh, A.J. Bard, Thermodynamic guidelines for the design of bimetallic catalysts for oxygen electroreduction and rapid screening by scanning electrochemical microscopy. M-Co (M: Pd, Ag, Au), *J. Am. Chem. Soc.* 127 (2005) 357-365.
- [⁴²] C.-L. Lin, C.M. Sánchez-Sánchez, A.J. Bard, Methanol tolerance of Pd-Co oxygen reduction reaction electrocatalysts using scanning electrochemical microscopy, *Electrochem. Solid-State Lett.* 11 (2008) B136-B139.
- [⁴³] R. O'Hayre, S.-W. Cha, W. Colella, F.B. Prinz, *Fuel Cells Fundamentals*, Wiley, New York, 2005.
- [⁴⁴] X. Yu, P.G. Pickup, Recent advances in direct formic acid fuel cells (DFAFC), *J. Power Sources* 182 (2008) 124-132.
- [⁴⁵] A.J. Bard, R. Parsons, J. Jordan (Eds.), *Standard Potentials in Aqueous Solution*, Marcel Dekker, New York, 1985, pp. 190-192.
- [⁴⁶] K. Jiang, H.-X. Zhang, S. Zou, W.-B. Cai, Electrocatalysis of formic acid on palladium and platinum surfaces: from fundamental mechanisms to fuel cell applications, *Phys. Chem. Chem. Phys.* 16 (2014) 20360-20376.
- [⁴⁷] J. Solla-Gullón, V. Montiel, A. Aldaz, J. Clavilier, Electrochemical and electrocatalytic behaviour of platinum-palladium nanoparticle alloys, *Electrochem. Commun.* 4 (2002) 716-721.

-
- [⁴⁸] J. Chang, L. Feng, C. Liu, W. Xing, X. Hu, An effective Pd-Ni₂P/C anode catalyst for direct formic acid fuel cells, *Angew. Chem. Int. Ed.* 53 (2014) 122-126.
- [⁴⁹] A. Sáez, J. Solla-Gullón, E. Expósito, A. Aldaz, V. Montiel, Electrochemical analysis of the performance of carbon supported Pd nanoparticles for direct formic acid fuel cells: from gold supported electrodes to catalyst-coated membranes, *Int. J. Electrochem. Sci.* 8 (2013) 7030-7043.
- [⁵⁰] F.J. Vidal-Iglesias, R.M. Arán-Ais, J. Solla-Gullón, E. Garnier, E. Herrero, A. Aldaz, J.M. Feliu, Shape-dependent electrocatalysis: formic acid electrooxidation on cubic Pd nanoparticles, *Phys. Chem. Chem. Phys.* 14 (2012) 10258-10265.
- [⁵¹] Z. Liu, L. Hong, M.P. Tham, T.H. Lim, H. Jiang, Nanostructured Pt/C and Pd/C catalysts for direct formic acid fuel cells, *J. Power Sources* 161 (2006) 831-835.
- [⁵²] O. Lugaresi, J.V. Perales-Rondón, A. Minguzzi, J. Solla-Gullón, S. Rondinini, J.M. Feliu, C.M. Sánchez-Sánchez, Rapid screening of silver nanoparticles for the catalytic degradation of chlorinated pollutants in water, *Appl. Catal. B* 163 (2015) 554-563.
- [⁵³] J. Solla-Gullón, V. Montiel, A. Aldaz, J. Clavilier, Synthesis and electrochemical decontamination of Platinum-Palladium nanoparticles prepared by water-in-oil microemulsion, *J. Electrochem. Soc.* 150 (2003) E104-E109.
- [⁵⁴] J. Solla-Gullón, A. Rodes, V. Montiel, A. Aldaz, J. Clavilier, Electrochemical characterisation of platinum-palladium nanoparticles prepared in a water-in-oil microemulsion, *J. Electroanal. Chem.* 554-555 (2003) 273-284.
- [⁵⁵] S. Trasatti, O.A. Petrii, Real surface area measurements in electrochemistry, *Pure Appl. Chem.* 63 (1991) 711-734.
- [⁵⁶] R. Woods, Chemisorption at electrodes in: A.J. Bard (Ed.), *Electroanalytical Chemistry Vol. 9*, Marcel Dekker, New York, 1976.

- [⁵⁷] M.A. Montiel, J. Solla-Gullón, C.M. Sánchez-Sánchez, Electrochemical reactivity and stability of platinum nanoparticles in imidazolium-based ionic liquids, *J. Solid State Electrochem.* 20 (2016) 1043-1052.
- [⁵⁸] D.A. Walsh, J.L. Fernández, J. Mauzeroll, A.J. Bard, Scanning electrochemical microscopy. 55. Fabrication and characterization of micropipet probes, *Anal. Chem.* 77 (2005) 5182-5188.
- [⁵⁹] F. Zhou, P.R. Unwin, A.J. Bard, Scanning electrochemical microscopy. 16. Study of second-order homogeneous chemical reactions via the feedback and generation/collection modes, *J. Phys. Chem.* 96 (1992) 4917-4924.
- [⁶⁰] R.N. Itoe, G.D. Wesson, E.E. Kalu, Evaluation of oxygen transport parameters in H₂SO₄-CH₃OH mixtures using electrochemical methods, *J. Electrochem. Soc.* 147 (2000) 24445-2450.
- [⁶¹] V. Grozovski, J. Solla-Gullón, V. Climent, E. Herrero, J.M. Feliu, Formic acid oxidation on shape-controlled Pt nanoparticles studied by pulsed voltammetry, *J. Phys. Chem. C* 114 (2010) 13802-13812.
- [⁶²] B. Gralec, A. Lewera, Catalytic activity of unsupported Pd-Pt nanoalloys with low Pt content towards formic acid oxidation, *Appl. Catal. B* 192 (2016) 304-310.
- [⁶³] C.A. Rice, A. Bauskar, P.G. Pickup, Recent advances in electrocatalysis of formic acid oxidation, in: M. Shao (ed.), *Electrocatalysis in Fuel Cells*, Springer-Verlag, London, 2013.
- [⁶⁴] X. Li, I.-M. Hsing, Electrooxidation of formic acid on carbon supported Pt_xPd_{1-x} (x=0-1) nanocatalysts, *Electrochim. Acta* 51 (2006) 3477-3483.
- [⁶⁵] S. Ait-Mohand, F. Henin, J. Muzart, Palladium(II)-mediated oxidation of alcohols using 1,2-dichloroethane as Pd(0) reoxidant, *Tetrahedron Lett.* 36 (1995) 2473-2476.
- [⁶⁶] D.R. Lide (Ed.), *CRC Handbook of Chemistry and Physics*, 74th ed., CRC Press, Boca Raton, 2000, pp. 16-24.